

Time lags and their association with the Boundary Layer structure in a Z source GX 349+2

Abhishek M.V.R.^{a,*}, Sriram K^a, Gouse SD^a

^aDepartment of Astronomy, Osmania University, , Hyderabad, 500049, , India

Abstract

Studying the cross-correlation function between the soft and hard X-ray emission in Neutron Star Low Mass X-ray Binaries provides crucial insight into the structure and dynamics of the innermost accretion regions. In this work, we investigate the CCF of the Z-source GX 349+2 using an XMM-Newton observation. We noted that asymmetric CCFs with lags of a few hundred seconds between soft and hard band LCs in the horizontal branch, whereas CCFs remained symmetric in normal and flaring branches. We also performed a CCF study during the flux transition duration and observed lags of the order of a few tens to hundreds of seconds. Monte Carlo simulations were performed to assess the robustness of these CCFs, confirming their significance at a 95% confidence level. Spectral analysis during the flux transitions further suggests that the inner accretion disk extends close to the last stable orbit. We propose that the observed hard lags arise from the readjustment of the boundary layer/coronal region located near the inner edge of the accretion disk. From the measured lags, we estimate the characteristic size of the boundary layer. We show that the observed lags could also be associated with the depletion timescale of the boundary layer with low viscosity.

Keywords: accretion, X-ray Binaries, Z-source, GX 349+2

1. Introduction

Neutron star low-mass X-ray binaries (NS-LMXBs) are particularly valuable laboratories for studying accretion physics under strong gravity, as the presence of a solid surface and often a Boundary Layer(BL) distinguishes them fundamentally from black hole systems. Despite decades of observational and theoretical work, several key aspects of the accretion process in NS-LMXBs remain poorly understood, including the geometry and evolution of the corona, the physical origin of spectral state transitions, and the coupling between the disk, boundary layer, and Comptonizing region.

NS-LMXBs are further classified based on the characteristic tracks they trace in Hardness–Intensity Diagrams (HIDs) into atoll and Z sources. Z sources exhibit three distinct branches in the HID: the Horizontal Branch (HB), Normal Branch (NB), and Flaring Branch (FB), which are generally associated with changes in mass accretion rate and spectral–timing properties. Only a small number of Z sources are known, and they are further subdivided according to their phenomenological behavior into 1) Sco-like sources, e.g., Sco X-1, GX 17+2, and GX 349+2 (Sco X-2) and 2) Cyg-like sources, e.g., Cyg X-2, GX 5–1, and GX 340+0 (1989).

GX 349+2 is a persistently bright NS-LMXB and a well-known member of the Sco-like subclass of Z sources (Hasinger & van der Klis (1989)). The source traces a characteristic Z-shaped pattern in Hardness–Intensity and Colour–Colour diagrams, primarily exhibiting the normal and flaring branches, while the horizontal branch is generally weak or absent, distinguishing it from Cyg-like Z sources (Kuulkers & van der

Klis (1995); O’Neill et al. (2002)). Extensive timing studies using RXTE have revealed strong low-frequency noise components and peaked variability in the ~ 3 –7 Hz range along the normal and flaring branches, with the timing properties evolving systematically along the Z track (O’Neill et al. (2002); Agrawal & Bhattacharyya (2003)). Additionally, twin kilohertz quasi-periodic oscillations at frequencies of $\nu \sim 712$ and ~ 978 Hz have been detected, indicating that the inner accretion flow extends close to the neutron star surface (Zhang et al. (1998)). Cross-correlation analysis between two energy band lightcurves provides us with timing information of which band leads/lags, giving us a crucial understanding of the hard and soft band photons emitting regions and their interaction, which could be manifesting in the form of the said lags/leads. Cross-correlation studies of this source using RXTE observations have revealed both soft and hard X-ray lags, ranging from a few seconds to several hundred seconds (Ding et al. (2016)). Broadband spectral analyses suggest that the X-ray emission of Sco X-2 is dominated by a combination of thermal emission from the accretion disk and BL, along with a Comptonized component originating from a hot corona, reflecting the complex accretion geometry in this system (Agrawal & Sreekumar (2003); Iaria et al. (2009); Lin et al. (2009); Ng et al. (2010)).

In this work, we use the XMM-Newton observations to perform a CCF analysis of the Z-source GX 349+2 (Sco X-2), with the aim of constraining the physical properties of the system through a combined temporal and spectral investigation.

2. Observations

The XMM-Newton observatory carries the European Photon Imaging Camera (EPIC), which consists of two MOS CCD

*Corresponding author. mvrabhishek@gmail.com (M.V.R. Abhishek)

detectors and one pn CCD detector. The EPIC instruments provide a field of view of approximately 30 arcmin and are sensitive over the energy range, 0.15–15.0 keV. Owing to the high brightness of GX 349+2, the MOS1 and MOS2 cameras were not operated during this observation to avoid photon pile-up effects. Consequently, only the EPIC-pn camera was used, operated in Timing mode with the medium optical blocking filter. The source was observed by XMM-Newton for a total exposure of 22.5 ks on 2008 March 19, between 16:42:41 UT and 22:58:55 UT (ObsID: 0506110101), during satellite revolution 1516. (Jansen et al. (2001))

3. Data Reduction and Analysis

X-ray light curves for GX 349+2 were extracted using the *evselect* task within the XMM-Newton Science Analysis Software (SAS). For the EPIC-pn camera operating in timing mode, we applied the standard event selection criteria (PATTERN ≤ 4) and *XMMEA_EP*. During the observation (ObsID: 0506110101), the EPIC-pn instrument experienced full scientific buffer conditions throughout, resulting in a low and highly variable effective live-time fraction per frame. To account for this effect, we applied the *epiclccor* task to correct the extracted LCs. This procedure applies the appropriate Good Time Intervals (GTIs), corresponding to periods when reliable flux measurements are obtained, and corrects for instrumental effects such as dead time and exposure variations, see (Iaria et al. (2009)).

Fig. 1 (left panel) shows the background-subtracted LC of the entire observation in the 0.8–10.0 keV energy band, and the shaded region depicts the HB, and different colours display the different branches (blue: FB, green: HB, orange: NB). To mitigate potential photon pile-up effects, we excluded the central bright RAW column (RAWX = 37) along with one adjacent column on either side (RAWX = 36 & 38). As evident from Fig. 1 (left panel), the source exhibits strong variability throughout the observation (see Iaria et al. 2009). The right panel of Fig. 1 displays the hardness–intensity diagram (HID), where the hardness ratio is defined as the ratio of count rates in the 2.0–10.0 keV and 0.8–2.0 keV energy bands.

For the detailed analysis, the total exposure of 22.5 ks was divided into 11 segments of approximately 2000 s each. We performed a CCF analysis between the soft (0.8–2.0 keV) and hard (2.0–10.0 keV) X-ray LCs using the *crosscorr* task from the XANADU data analysis package. The cross-correlations were computed with a 50 s bin and applied to all the segments of the observation. Asymmetric CCFs exhibiting non-zero lags, accompanied by relatively low cross-correlation coefficients, were detected in the segments associated with the horizontal branch of the HID (Fig. 1, shaded region). In each row, the left panel shows the soft-band LC, the middle panel displays the hard-band LC, and the right panel presents the corresponding CCF for each of the sections (see Fig. 2). These segments are hereafter referred to as Sections 1 & 2.

In contrast to Sections 1 and 2, shown in Fig. 2, the CCFs shown in Fig. 3 are highly symmetric and peak at zero lag,

indicating a near simultaneous variation of the soft and hard X-ray emissions. These segments are predominantly associated with the normal branch (NB) and flaring branch (FB) of the HID.

In a separate division of data covering the transition windows of approximately 2200 s each, see Fig. 4 (top). The highlighted windows are where the non-zero lags with asymmetric CCFs were found and these windows are referred to as Sections A, B and C, hereafter to perform spectral studies.

3.1. Validation of Lags

To validate the lags found from the original observations CCF analysis, in Sections 1 and 2 as well as Sections A, B and C, we performed simulations by generating 10,000 pairs of synthetic soft and hard LCs, which were produced by introducing random variations to each data point within the standard deviation of the corresponding observed LC, thereby preserving the intrinsic variability characteristics of the source (Gouse et al. (2025a, 2025b)).

CCF functions were then computed for each simulated LC pair. Each resulting CCF was fitted with a composite model consisting of a linear baseline plus a Gaussian component (line + Gaussian + line) to determine the peak cross-correlation coefficient and estimate the associated lag. The histogram of these estimated lags was fitted with a Gaussian to validate the observed lag; plots are shown in Fig. 5 & 6(left panels of each row).

3.2. Cross Correlation Confidence Interval

Soft and hard LCs were simulated using the method proposed by Timmer & Konig (1995), which is widely used to produce stochastic variability in time series characterized by power-law noise. Using the observed power spectral properties of the source, $\Gamma_{PSD} = 2.1$, and the mean same as the original LC, we generated 10,000 simulated LCs independently for the soft (0.8–2.0 keV) and hard (2.0–10.0 keV) energy bands (Gouse et al. (2025a, 2025b)). The CCF was then computed for each pair of simulated LCs in order to construct the statistical distribution of CCFs and derive the corresponding 95% confidence intervals (Fig. 5 & 6, right panels). The simulated LCs were generated using the AstroML (2012) time-series module. In Fig. 5 & 6 (right panels), the CCFs corresponding to the 10,000 simulated LCs are shown in blue, while the observed CCF is overlaid in red. The dotted black curves represent the 95% confidence limits derived from the simulations. This procedure is essential to demonstrate that the asymmetric CCFs and associated time lags detected in the data are not the result of random fluctuations, but instead arise from intrinsic temporal incoherence between the soft and hard X-ray emitting regions.

4. Spectrum Analysis

The spectra were extracted in the energy range 0.8–10 keV during the time intervals corresponding to the detected lags for sections A, B, and C. For the source extraction, we used RAWX columns 29–45, excluding the central bright columns 37 and

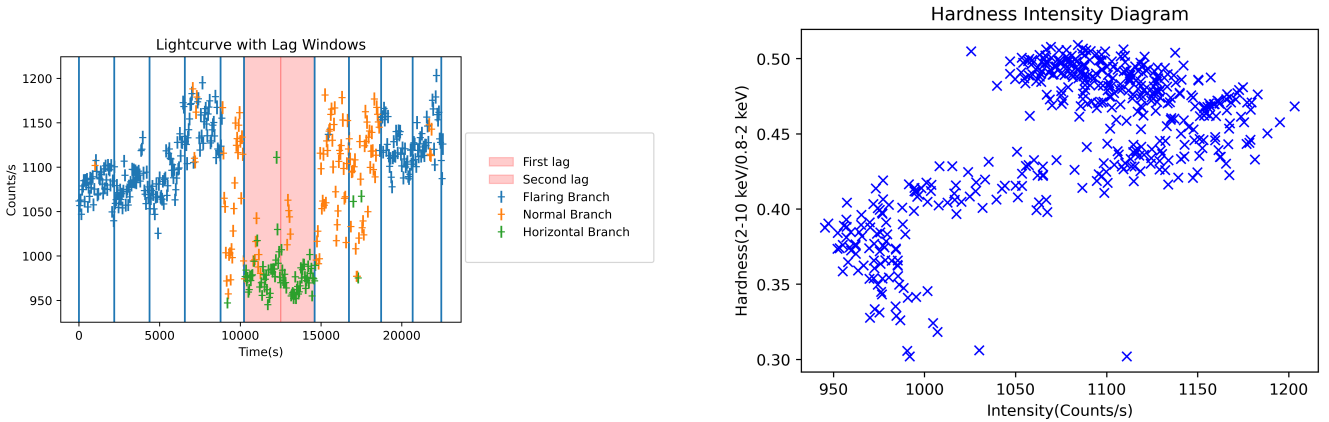


Figure 1: The left panel is a plot of the LC in the 0.8-10 keV band, with the sections where lags are found (horizontal branch) highlighted; the right panel is a plot of the Hardness Intensity Diagram of the observation.

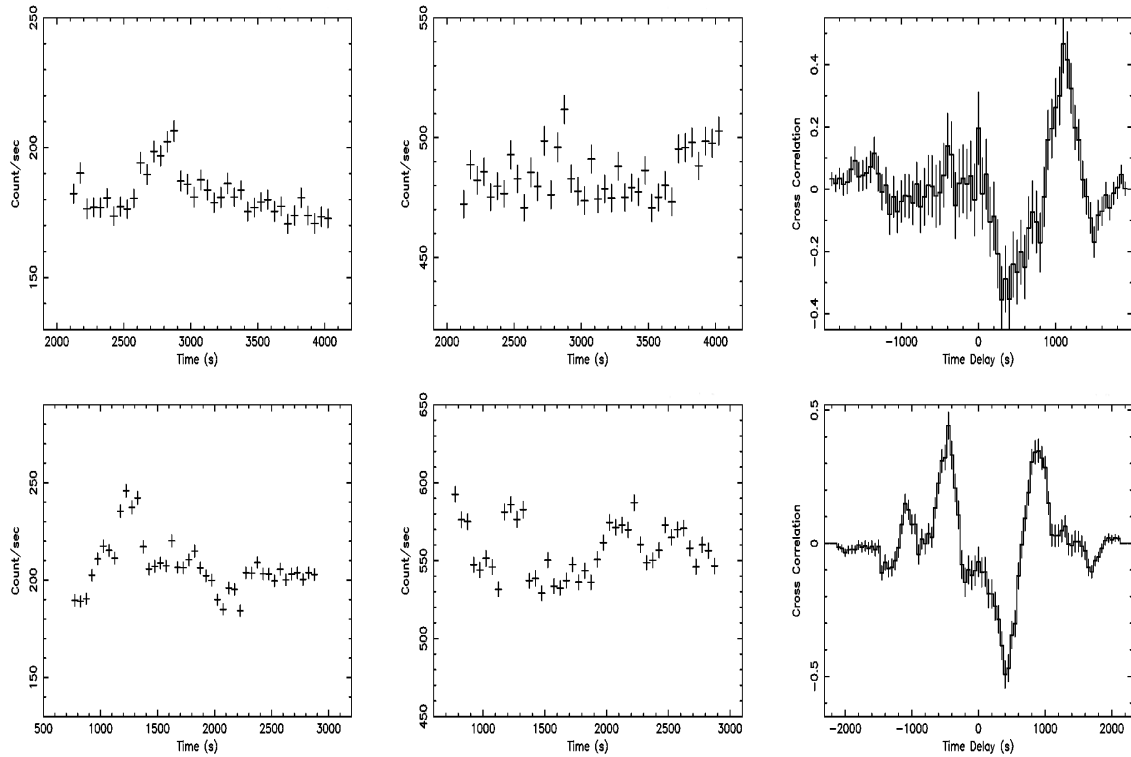


Figure 2: First two sub-plots in each row are the soft and hard LCs, respectively, and the third is the CCF plot. HB1 and HB2.

38 to mitigate the effects of pile-up (Iaria et al. (2009)). The background spectra were extracted from RAWX columns 2–18. In accordance with the XMM-Newton User Handbook (May 2016), we applied the selection criterion (*FLAG*=0) to ensure robust spectral analysis. The EPIC-pn spectrum shows calibration issues between the energy band 2 – 2.5 keV, due to the presence of the Au edge at \sim 2.3 keV, we excluded the 2.1 – 2.5 keV band when extracting the spectrum, Iaria et al. 2009. The spectra were grouped to a minimum of 25 counts per bin.

Spectral fitting was performed using XSPEC version 12.12.1. Initially, the spectra were modeled with the $T_{abs} \times (bbodyrad + Gaussian + power-law)$ (Model 1). The *bbodyrad* component

represents blackbody emission, with its normalization proportional to the emitting surface area. Specifically, the normalization provides an estimate of the radius of the blackbody emitter interpreted here as the neutron star according to $N_{bbr} = \frac{R_{km}^2}{D_{10}^2}$. D_{10} is the source distance in units of 10 kpc. We adopt a source distance of 9.2 kpc (Coughenour et al. 2018). The best-fit spectral parameters for the first and last 500 s of sections A, B, and C are listed in Table 1. Fig. 7 shows the spectral fit for Section A.

The spectrum was also fitted with the model $T_{abs} * (bbodyrad + diskbb + Gaussian)$ (Model 2), as

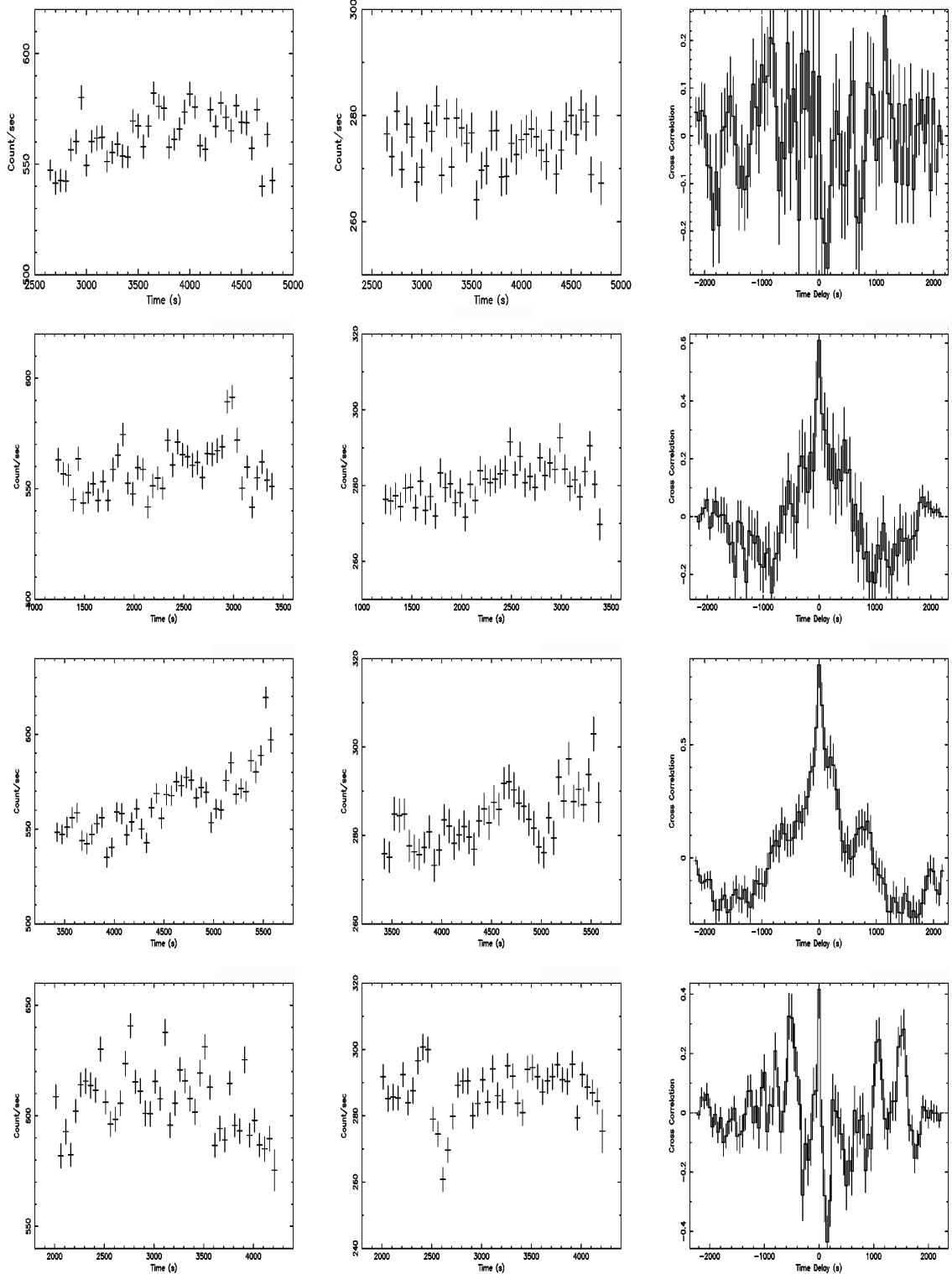


Figure 3: The first two plots in each row are the soft and hard LCs, respectively, and the third is the CCF. All rows belong to the FB.

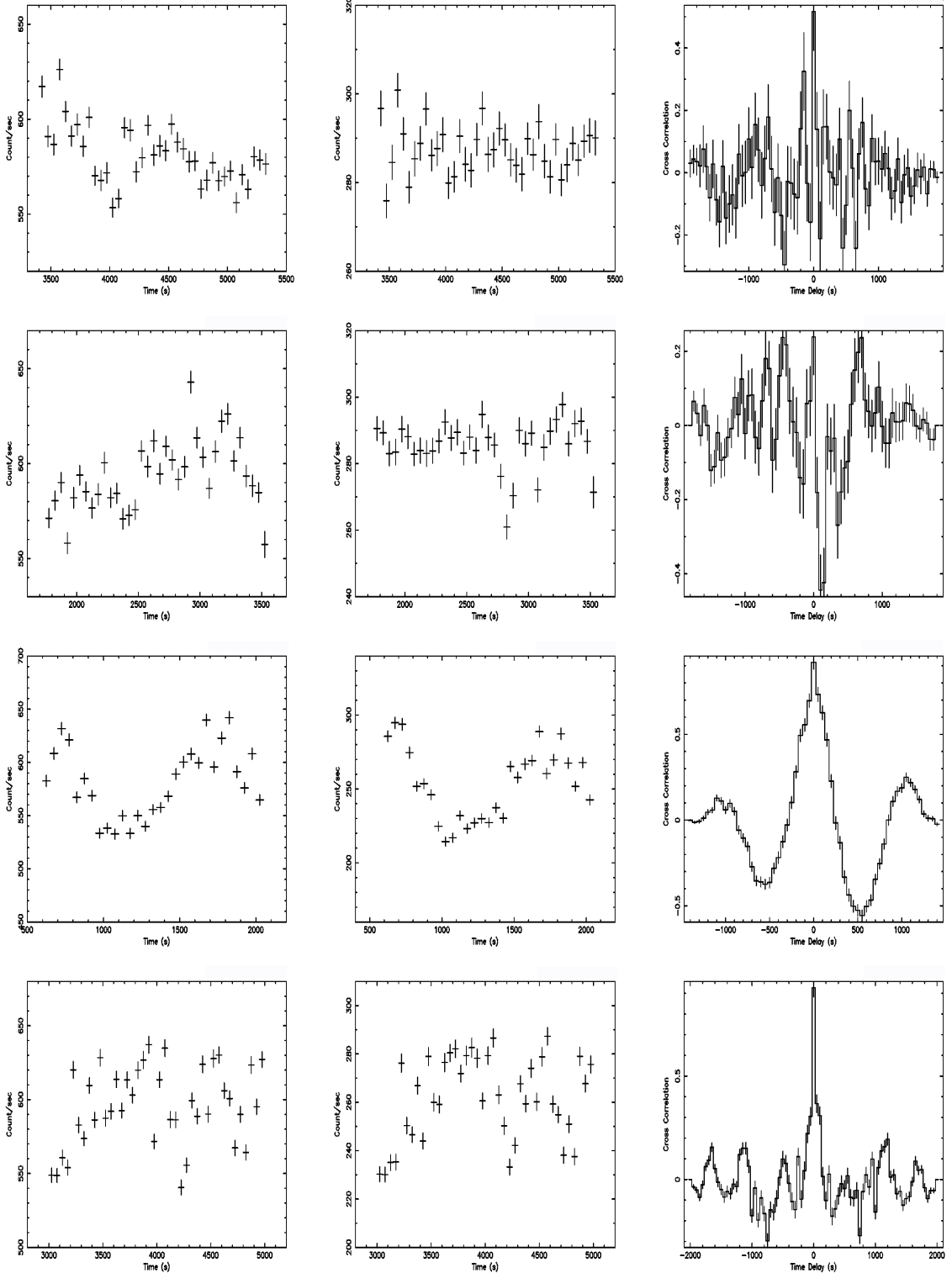


Figure 3: Continued.. The top 2 rows display the LCs and CCFs of the FB, and the bottom 2 panels show the NB section.

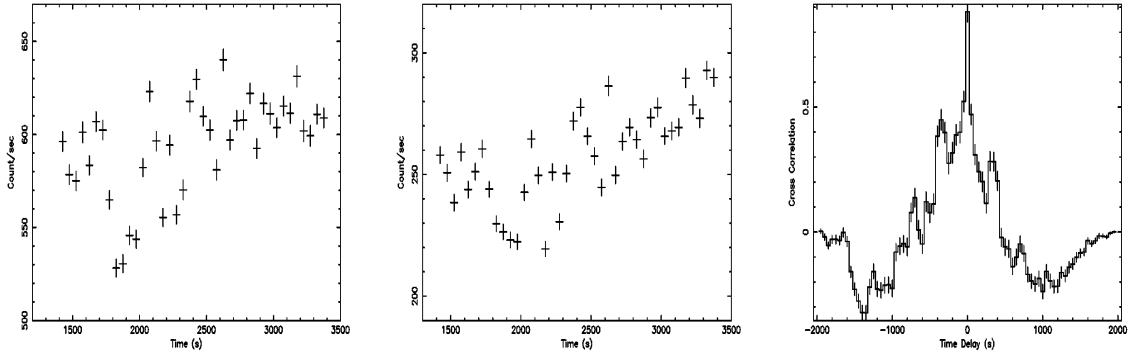


Figure 3: continued.. NB section LCs and CCF.

done by Coughenour (2018), where they used this as the initial model to fit the data from NuStar for the source GX 349+2, and tried to model it separately during each branch of its HID diagram. We applied this model as well to sections A, B and C, and reported the best-fit parameters for the same in Table 2. The hydrogen column density of model T_{babs} for both models has been set to $N_H = 0.8 \times 10^{22}$ atoms cm $^{-2}$ (Iaria et al. 2009).

Markov Chain Monte Carlo (MCMC) simulations were performed to investigate the posterior probability distributions of the model parameters. The simulations were carried out using the Goodman–Weare algorithm, with a total chain length of 200,000 steps and a burn-in phase of 50,000 steps. Fig. 8 presents the joint confidence (contour) plots of the key parameters, illustrating their variations across sections A, B, and C, where significant lags were detected. The contours indicate that the photon index, Γ , exhibits statistically significant variations in sections A and C. This behaviour suggests changes in the radiative and/or geometric properties of the BL or the corona during these intervals. On the other hand, the *Norm* of *bbodyrad* showed a larger variation in all the sections A, B and C, suggesting that the BL size has varied during the said windows(since *Norm* of *bbodyrad* gives the direct measure of Radius of the source, see tables 3 & 4).

Using the normalization values of the *bbodyrad* component from the spectral fits, we find the radius of the body (NS) along with Ω_k (Keplerian rotation frequency), Ω_{NS} (Neutron star spin frequency), Ω (at various distances), which will be used to find the t_{depl} following the relation, $t_{depl} = \frac{(\Omega - \Omega_{NS})}{\alpha(\Omega_k^2 - \Omega^2)}$. Table 3 & 4 shows the t_{depl} values for $\alpha = 10^{-7}$ (discussed in the later sections).

5. Discussion

For the first time, we performed CCF analysis on the soft (0.8-2.0 keV) and hard LCs (2-10 keV) using EPIC-pn data of the XMM-Newton observatory for the source GX 349+2. The CCFs revealed time lags of a few hundred seconds during the horizontal branch (HB) as seen in sections 1 & 2. We find that the CCFs associated with the HB are highly asymmetric and exhibit significant lags. In contrast, those corresponding to the normal and flaring branches (NB and FB) are symmetric

and show no statistically measurable lags. Ding et al. (2016) investigated soft-hard X-ray time lags in the Z-sources GX 349+2 using RXTE observations. They reported significant lags, typically ranging from tens to a few hundred seconds, predominantly in the HB, while little or no lag was detected in the normal and flaring branches, and they interpreted lags as the viscous timescale in the inner accretion flow, possibly linked to variations in the corona. EPIC-pn data allows us to use the soft energy band 0.8-2.0 keV, which was not possible with PCA/RXTE. Recently, Gouse et al. (2025a, 2025b) demonstrated that RXTE observations of Sco X-1 exhibit a clear dichotomy in soft-hard X-ray CCFs, which is closely associated with distinct modes of radio jet ejection. They found that asymmetric CCFs, characterized by weak correlations and time lags of a few hundred seconds, occur during ballistic (lobe) jet episodes and are accompanied by flat-topped noise and the absence of coherent oscillations in the power density spectrum (PDS). In contrast, symmetric CCFs occur during normal and flaring branch states, and coincide with ultra-relativistic flow (URF) events, and exhibit persistent oscillations (NBO/NBO+HBO/FBO). These results suggest two states of the inner accretion flow: ballistic jet launching disrupts the BL and/or corona, producing delayed CCFs and suppressing oscillations within a region of size ~ 10 –40 km, whereas URFs are associated with a stable, steady accretion configuration. Thus, CCF asymmetry provides a robust diagnostic of jet–disk coupling in Sco X-1. We also noted a very similar scenario in the case of GX 349+2, where asymmetric CCFs were associated with HB and relatively symmetric CCFs in the FB and NB. This analogy displays that the inner accretion disk was disrupted, probably due to the mechanism that launched the jet.

We also performed CCFs during the flux transition corresponding to branch variations in HID (Sections A, B, and C; See Fig. 5 & 6). We again noted asymmetric CCFs with lags having more than 95% significance during these phases, clearly indicating that the BL/corona or inner region of the accretion disk has varied. This is supported by the observation that both the parameters kT_{bbr} and N_{bbr} varied throughout the sections of A, B, and C, whereas Γ changed from 1.70 ± 0.03 to 1.60 ± 0.03

Table 1: Best fit parameters evaluated using the model $Tbabs * (bbodyrad + powerlaw + gaussian)$. The $Fe_{K\alpha}$ line is fixed at 6.7 keV and the N_H value fixed at 0.8×10^{22} atoms cm^{-2} .

Parameter	Section A		Section B		Section C	
	First 500s	Last 500s	First 500s	Last 500s	First 500s	Last 500s
$kT_{bbr}(keV)$	$1.09^{+0.03}_{-0.03}$	$1.20^{+0.03}_{-0.03}$	$1.41^{+0.04}_{-0.04}$	$1.27^{+0.09}_{-0.09}$	$1.29^{+0.03}_{-0.03}$	$1.15^{+0.03}_{-0.03}$
N_{bbr}	295^{+22}_{-20}	223^{+17}_{-15}	114^{+8}_{-3}	164^{+74}_{-34}	175^{+12}_{-11}	275^{+18}_{-16}
Γ_{pl}	$1.70^{+0.03}_{-0.03}$	$1.60^{+0.03}_{-0.03}$	$1.40^{+0.04}_{-0.04}$	$1.37^{+0.15}_{-0.05}$	$1.54^{+0.04}_{-0.03}$	$1.58^{+0.03}_{-0.03}$
N_{pl}	$1.53^{+0.03}_{-0.03}$	$1.51^{+0.03}_{-0.03}$	$1.08^{+0.02}_{-0.02}$	$0.97^{+0.04}_{-0.05}$	$1.31^{+0.03}_{-0.03}$	$1.54^{+0.03}_{-0.03}$
$Flux_{bbr}$	4.34	4.72	4.43	4.3	4.96	4.96
$Flux_{pl}$	8.63	9.71	8.92	8.39	9.06	8.64
$Flux_{Total}$	12.97	14.43	13.35	12.69	14.02	13.6
Luminosity	1.31	1.43	1.40	1.31	1.41	1.41
χ^2/dof	602/630	627/660	685/671	694/677	651/660	684/642

bbr: bbodyrad, pl: powerlaw, Flux here has the units of $10^{-9} ergcm^{-2}s^{-1}$, Luminosity has the units of $10^{38} erg/s$.

Table 2: Best Fit parameters using the model $Tbabs * (bbodyrad + diskbb + gaussian)$. The $Fe_{K\alpha}$ line is fixed at 6.76keV and the N_H value fixed at 0.8×10^{22} atoms cm^{-2} .

Parameter	Section A		Section B		Section C	
	First 500s	Last 500s	First 500s	Last 500s	First 500s	Last 500s
$kT_{bbr}(keV)$	$1.87^{+0.10}_{-0.08}$	$1.89^{+0.08}_{-0.07}$	$2.04^{+0.14}_{-0.09}$	$2.11^{+0.06}_{-0.04}$	$1.88^{+0.08}_{-0.06}$	$1.75^{+0.06}_{-0.05}$
N_{bbr}	68^{+15}_{-15}	81^{+15}_{-15}	60^{+15}_{-17}	51^{+1}_{-1}	86^{+14}_{-16}	100^{+15}_{-16}
kT_{in} (keV)	$1.15^{+0.09}_{-0.08}$	$1.14^{+0.1}_{-0.08}$	$1.31^{+0.22}_{-0.14}$	$1.46^{+0.07}_{-0.06}$	$1.14^{+0.12}_{-0.09}$	$1.04^{+0.07}_{-0.06}$
N_{dbb}	$195.80^{+44.94}_{-39.95}$	$192.98^{+46.03}_{-41.25}$	$89.97^{+35.61}_{-31.61}$	$63.03^{+8.10}_{-7.84}$	$164.82^{+44.67}_{-40.77}$	$265.72^{+55.45}_{-49.71}$
$Flux_{bbr}$	7.04	8.83	8.33	8.01	9.17	8.41
$Flux_{dbb}$	6.19	5.79	4.84	5.39	4.92	5.46
$Flux_{Total}$	13.2	14.6	13.2	13.4	14.1	13.9
Luminosity	1.34	1.48	1.33	1.36	1.43	1.41
χ^2/dof	621/630	648/660	699/671	722/677	661/660	699/642

bbr: bbodyrad, dbb: diskbb, Flux is the units of $10^{-9} ergcm^{-2}s^{-1}$, Luminosity has the units of $10^{38} erg/s$.

Table 3: Table for t_{depl} (s) values at various radius for Model 1.

Section	Radius(km)	\dot{m} (g/s)	R_{BL} (km)	Ω_k (Hz)	$t_{depl,27km}$	$t_{depl,23km}$	$t_{depl,21km}$	$t_{depl,20km}$
A First	15.79	1.12	34.12	1093.64	230.32	433.81	639.18	809.33
Last	13.76	1.08	31.25	1343.95	205.37	379.41	547.11	680.07
B First	9.82	0.72	20.39	2230.63	33.16	54.12	69.22	78.6
Last	11.79	0.82	24.18	1695.02	71.38	119.59	156.52	180.54
CFirst	12.19	0.93	26.69	1612.53	101.2	173.13	231	270.2
Last	14.23	1.07	31.51	1278.23	163.12	291.9	406.96	492.15

units of t_{depl} are in seconds, Radius here is the NS radius from N_{bbr} .

Table 4: Table for t_{depl} (s) values at various radius for model 2.

Section	Radius(km)	\dot{m} (g/s)	R_{BL} (km)	Ω_k (Hz)	$t_{depl,27km}$	$t_{depl,23km}$	$t_{depl,21km}$	$t_{depl,20km}$
A First	7.39	5.32	15.01	3418.35	194.89	315.14	399.93	451.61
Last	8.29	6.61	17.96	2873.20	278.28	452.51	577.0	653.64
B First	7.24	5.19	14.66	3523.86	183.17	295.95	375.34	423.64
Last	6.58	4.80	13.42	4067.15	136.83	220.40	278.79	314.13
C First	8.58	6.59	18.21	2730.98	309.0	503.51	643.17	729.50
Last	9.0	6.80	18.98	2541.66	358.58	586.27	751.04	853.50

units of t_{depl} are in seconds, Radius here is the NS radius from N_{bbr} .

only in section A (see Table 1). Both lags and spectral variation during the transitions clearly suggest that the BL/corona has changed its radiative and physical structures. We suggest that if such structural variation had not happened, the CCFs would have been highly symmetric.

5.1. Relation between lags and BL

The observed soft-hard X-ray lag of $t \sim 200$ s in GX 349+2 can be interpreted as the mechanical readjustment timescale of the BL and the inner disk. In a previous study of a different Z source, it was noted that such time lags were seen and interpreted as the readjustment time scale of corona or BL (Sriram et al. (2013); Sriram et al. (2019); Malu et al. (2021); Chiranjeevi & Sriram (2022); Chiranjeevi et al. (2023)). Assuming that the lag arises due to viscous redistribution of mass and angular momentum over a small radial extent $\Delta R \ll R$, the effective viscous timescale is related to the observed lag via

$$\Delta t \sim \frac{3}{2} \frac{\Delta R}{R} t_{\text{visc}}, \quad (1)$$

where the viscous timescale t_{visc} at radius R is given by the standard α -disk prescription

$$t_{\text{visc}} \sim \frac{1}{\alpha} \left(\frac{R}{H} \right)^2 \frac{1}{\Omega_K}, \quad \Omega_K = \sqrt{\frac{GM}{R^3}}. \quad (2)$$

Here, H is the scale height of the BL, Ω_K the Keplerian angular frequency, and α the dimensionless viscosity parameter. Solving for α in terms of the observed lag yields

$$\alpha \sim \frac{3}{2} \frac{\Delta R}{R} \frac{1}{\Delta t} \left(\frac{R}{H} \right)^2 \frac{1}{\Omega_K}. \quad (3)$$

Using values for a neutron star with $R \sim 15$ km, $\Delta R \sim 2$ km, $H/R \sim 0.1$, and $\Omega_K \sim 1.2 \times 10^4$ s⁻¹, we obtain

$$\alpha \sim 8 \times 10^{-6}. \quad (4)$$

This extremely low effective viscosity indicates that the mechanical adjustment of the BL proceeds much more slowly than standard turbulent viscosity ($\alpha \sim 0.01$ – 0.1) (Babkovskia, Brandenburg, & Poutanen (2008)). Physically, this does not imply that the microscopic viscosity is unrealistically small; rather, it reflects the slower angular momentum transport in the BL, potentially mediated by radiative viscosity, magnetic stresses, or global coupling with the inner disk and corona. Such slow readjustment naturally explains the observed soft-hard lag on timescales of hundreds of seconds. Using the normalization values of the *bbbodyrad* component from the spectral fits, we find the radius of the body (NS) along with Ω_k (Keplerian rotation frequency), Ω_{NS} (Neutron star spin frequency), Ω (at various distances), which will be used to find the t_{depl} following the relation, $t_{\text{depl}} = \frac{(\Omega - \Omega_{NS})}{\alpha(\Omega_k^2 - \Omega^2)}$ (Abolmasov & Poutanen (2021)). Table 3 & 4 shows us the t_{depl} values for α value of 10^{-7} . The calculated time scales of t_{depl} are in agreement with those found in the CCF of the source.

Abolmasov & Poutanen (2021) showed that for α values of 10^{-7} the t_{depl} value turns out to be 740 s and lower for $\alpha = 10^{-6}$,

these lags are well in agreement with the scales of lags observed in the source GX349+2, hence the BL mechanical adjustments can be associated to the lags observed in this source. Such time scales were seen in an atoll source 4U 1728-34, the depletion associated with low $\alpha \leq 10^{-7}$ (Chiranjeevi et al. (2023)).

As discussed above the lags could be due to physical readjustment of the BL, we estimated the size of the BL using the following relation (Popham & Sunyaev (2001)).

$$\log(R_{BL} - R_{NS}) \sim 5.02 + 0.245[\log(\frac{\dot{M}}{10^{-9.85} M_{\odot} \text{yr}^{-1}})] \quad (5)$$

where \dot{M} is found using the equation $L = \frac{GM_{NS}\dot{M}}{R}$, where M_{NS} is the mass of the neutron star ($= 1.4M_{NS}$) M_⊙ and radius R is obtained from the Norm of *bbbodyrad* from the spectral fit along with luminosity (see Table 1 and 2). Using equation 5, we obtained the size of BL ranging from 20–34 km using Model 1, and 13–15 km using Model 2 (see Tables 3 & 4). It matches the BL Radius estimated by Coughenour et al. (2018), where they found BL would extend from 19.0 to 40 km.

Iaria et al. (2009) showed that GX 349+2 hosts an extended accretion disk corona (ADC) spanning several tens to hundreds of kilometres, a result later supported by the systematic ADC framework presented by Church et al. (2012). Recent X-ray polarization measurements of GX 349+2 reveal a polarization angle difference of 60° between the disk and Comptonized emission components, which can be explained by the presence of a boundary/spreading layer or an extended accretion disk corona (La Monaca et al. (2025)). Furthermore, Ludlam et al. (2025), using XRISM observations, independently reported evidence for a similarly extended coronal structure in the NS-LMXB, GX 340+0.

Within the accretion disk corona (ADC) framework, the observed ~ 200 s soft-hard lag cannot be attributed to light travel or Comptonization delays. Instead, it probably arises from the slow viscous readjustment of an extended corona in response to changes in the inner accretion flow. For a geometrically thick ADC extending over tens of kilometres, a low effective viscosity ($\alpha_{\text{eff}} \sim 10^{-3}$ – 10^{-4}) yields adjustment timescales of hundreds of seconds, consistent with the observed lags. For $\Delta R = \alpha(H/R)^2 v_k \Delta t$, where Δt is observed lag, v_k Keplerian velocity, assuming a $H/R = 0.1$, $\Delta t = 200$ s, and $\alpha = 10^{-3}$ to -4 , we get $\Delta R \sim 30$ km – 300 km. This supports a picture in which the lag reflects the dynamical response of the disk-corona system rather than instantaneous radiative processes.

6. Conclusion

This study presents a comprehensive timing and spectral analysis of the NS-LMXB GX 349+2 (Sco X-2), covering the full evolution of the source along the Z-track in the hardness–intensity diagram (HID), with the source spending most of the observation time in the flaring branch (FB). For the first time, Cross-correlation function analysis using EPIC-pn data between soft and hard X-ray LCs revealed both correlated and

anti-correlated hard lags in several segments in this source. The main findings of this work are summarized below:

1. We noted a branch-dependent CCF behavior. Asymmetric CCFs exhibiting significant time lags are observed exclusively during the horizontal branch (HB). In contrast, the normal branch (NB) and flaring branch (FB) are characterized by highly symmetric CCFs with no statistically significant delays between the soft and hard bands.

2. The symmetric CCFs seen in the NB and FB likely indicate a stable accretion geometry in the inner disk region, where soft and hard photon intensity variations maintain temporal coherence. The asymmetric CCFs with measurable lags in the HB suggest the presence of instabilities in the inner accretion flow, possibly linked to episodic jet activity similar to Sco X-1 (Motta & Fender 2019). Such a scenario is consistent with the known association of the HB with radio jet emission, although simultaneous radio observations would be required to confirm this interpretation for GX349+2.

3. We noted lags during flux transitions, as well. During transitions between different Z-track branches, asymmetric CCFs reappear with measurable time lags. This behavior points to a variable emission component in the innermost accretion region, most plausibly the BL and/or corona. The observed delays may represent the readjustment timescale of the varying physical structure in this region as the accretion flow reorganizes. This is further emphasized by the change in the *Norm* parameter of *bbodyrad* observed in the spectral fitting and subsequently validated by the MCMC simulations.

4. We propose that the presence of these lags requires a relatively low effective viscosity in the inner accretion flow, allowing structural changes to propagate on observable timescales. This interpretation is consistent with the theoretical framework presented by Abolmasov & Poutanen (2021), where viscous timescales in radiation pressure-dominated regions can produce delayed responses between different emission components.

A simultaneous study in the X-ray and radio band of this source would provide an important view on the relation between the inner-accretion region and the jet base formation, as studied by Gouse et al. (2025a, 2025b) and Motta & Fender (2019). This would give a better understanding of the source's inner accretion disk geometry, structure and a coronal geometry, i. e. compact or extended corona scenario.

References

Abolmasov, P., Poutanen, J., 2021. Mechanical model of a boundary layer for the parallel tracks of kilohertz quasi-periodic oscillations in accreting neutron stars. *Astronomy & Astrophysics* 647, A45.

Agrawal, V., Sreekumar, P., 2003. X-ray spectral evolution of low-mass x-ray binary gx 349+ 2. *Monthly Notices of the Royal Astronomical Society* 346, 933–939.

Babkovskaia, N., Brandenburg, A., Poutanen, J., 2008. Boundary layer on the surface of a neutron star. *Monthly Notices of the Royal Astronomical Society* 386, 1038–1044.

Chiranjeevi, P., Sriram, K., Malu, S., Agrawal, V.K., 2023. Detection of lags in an atoll source 4u 1728-34 using astrosat. *Astrophysics and Space Science* 368, 77.

Church, M., Gibiec, A., Bałucińska-Church, M., Jackson, N., 2012. Spectral investigations of the nature of the scorpius x-1 like sources. *Astronomy & Astrophysics* 546, A35.

Coughenour, B.M., Cackett, E.M., Miller, J.M., Ludlam, R.M., 2018. A nustar observation of the low-mass x-ray binary gx 349+ 2 throughout the z-track. *The Astrophysical Journal* 867, 64.

Ding, G., Zhang, W., Wang, Y., Li, Z., Qu, J., Huang, C., 2016. The cross-correlation analysis in z source gx 349+ 2. *Monthly Notices of the Royal Astronomical Society* 455, 2959–2968.

Gouse, S., Abhishek, M., Sriram, K., 2025a. Asymmetric cross-correlation functions with delays in sco x-1: evidence of possible jet triggering. *Astrophysics and Space Science* 370, 1–18.

Gouse, S., Lahiri, D., Sriram, K., 2025b. Association of x-ray cross correlation function and radio jet emission in the z-source sco x-1. *Research in Astronomy and Astrophysics* 25, 115009.

Iaria, R., D'Aí, A., Di Salvo, T., Robba, N., Riggio, A., Papitto, A., Burderi, L., 2009. A ionized reflecting skin above the accretion disk of gx 349+ 2. *Astronomy & Astrophysics* 505, 1143–1151.

Jansen, F., Lumb, D., Altieri, B., Clavel, J., Ehle, M., Erd, C., Gabriel, C., Guainazzi, M., Gondoin, P., Much, R., et al., 2001. Xmm-newton observatory-i. the spacecraft and operations. *Astronomy & Astrophysics* 365, L1–L6.

La Monaca, F., Di Marco, A., Zelati, F.C., Bobrikova, A., Ludlam, R.M., Poutanen, J., Marino, A., Li, S., Xie, F., Feng, H., et al., 2025. X-ray spectropolarimetric characterisation of the z source gx 340+ 0 in the normal branch. *Astronomy & Astrophysics* 702, A101.

Lin, D., Remillard, R.A., Homan, J., 2009. Spectral states of xte j1701- 462: Link between z and atoll sources. *The Astrophysical Journal* 696, 1257.

Ludlam, R.M., Ballhausen, R., Chakraborty, P., Costantini, E., Corrales, L., Hall, H., Kilbourne, C.A., Moutard, D.L., Nakagawa, T., Porter, F.S., et al., 2025. The structure of the relativistic fe line in gx 340+ 0 as viewed with xrism/resolve, nicer, and nustar. *Publications of the Astronomical Society of Japan* 77, S117–S130.

Malu, S., Sriram, K., Harikrishna, S., Agrawal, V.K., 2021. Exploring the inner-disc region of the atoll source 4u 1705-44 using astrosat's sxt and laxpc observations. *Monthly Notices of the Royal Astronomical Society* 506, 6203–6211.

Motta, S., Fender, R., 2019. A connection between accretion states and the formation of ultrarelativistic outflows in a neutron star x-ray binary. *Monthly Notices of the Royal Astronomical Society* 483, 3686–3699.

Ng, C., Díaz Trigo, M., Cadolle Bel, M., Migliari, S., 2010. A systematic analysis of the broad iron k alpha line in neutron star lmxbs with xmm-newton. *A&A* 522, A96.

O'Neill, P., Kuulkers, E., Sood, R., Van Der Klis, M., 2002. The x-ray fast-time variability of sco x-2 (gx 349+ 2) with rxte. *Monthly Notices of the Royal Astronomical Society* 336, 217–232.

Popham, R., Sunyaev, R., 2001. Accretion disk boundary layers around neutron stars: X-ray production in low-mass x-ray binaries. *The Astrophysical Journal* 547, 355.

Sriram, K., Malu, S., Choi, C., 2019. Constraining the coronal heights and readjustment velocities based on the detection of a few hundred seconds delays in the z source gx 17+ 2. *The Astrophysical Journal Supplement Series* 244, 5.

Sriram, K., Rao, A., Choi, C., 2013. A spectral study of the rapid transitions of type-b quasi-periodic oscillations in the black hole transient xte j1859+ 226. *The Astrophysical Journal* 775, 28.

Sriram, K., et al., 2022. Anticorrelated lags in a neutron star z source gx 5-1: Astrosat's view. *Monthly Notices of the Royal Astronomical Society* 516, 2500–2513.

Timmer, J., Koenig, M., 1995. On generating power law noise. *Astronomy and Astrophysics*, v. 300, p. 707 300, 707.

van der Klis, M., 1989. The Z/atoll Classification, in: Hunt, J., Battrick, B. (Eds.), *Two Topics in X-Ray Astronomy*, Volume 1: X Ray Binaries. Volume 2: AGN and the X Ray Background, p. 203.

van der Klis, M., 1995. Rapid aperiodic variability in X-ray binaries., in: *X-ray Binaries*, pp. 252–307.

Vanderplas, J., Connolly, A., Ivezić, Ž., Gray, A., 2012. Introduction to astroml: Machine learning for astrophysics, in: Conference on Intelligent Data Understanding (CIDU), pp. 47 –54. doi:[10.1109/CIDU.2012.6382200](https://doi.org/10.1109/CIDU.2012.6382200).

Zhang, W., Strohmayer, T., Swank, J., 1998. Discovery of two simultaneous kilohertz quasi-periodic oscillations in the persistent flux of gx 349+ 2. *The Astrophysical Journal* 500, L167.

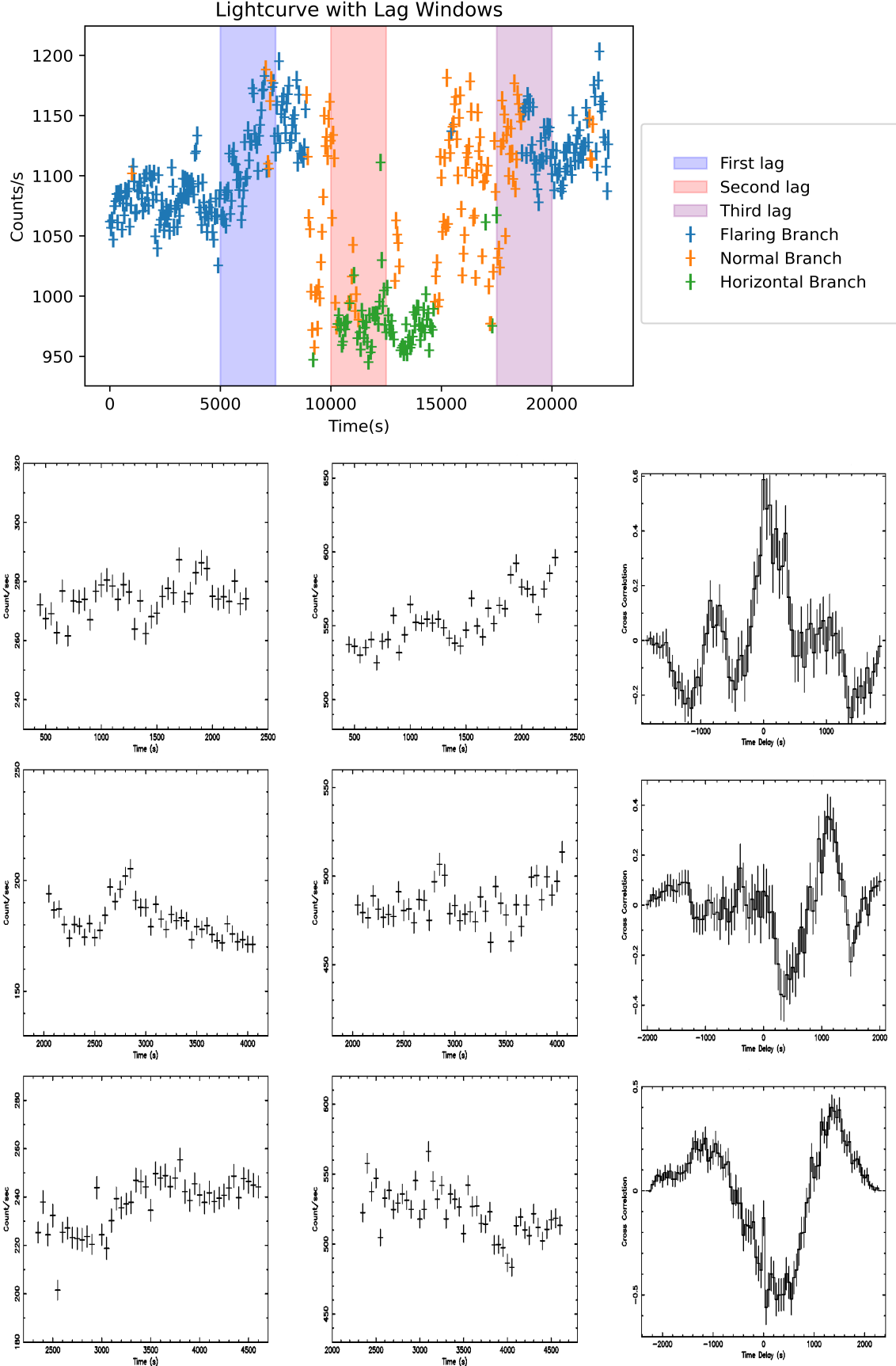


Figure 4: This first plot is the entire observation's LC with Sections A, B, and C highlighted. In the following plots, the first two images in each row are the soft and hard LCs, respectively, and the third is the CCF plot. Row 2, 3 and 4 belong to Sections A, B and C, respectively.

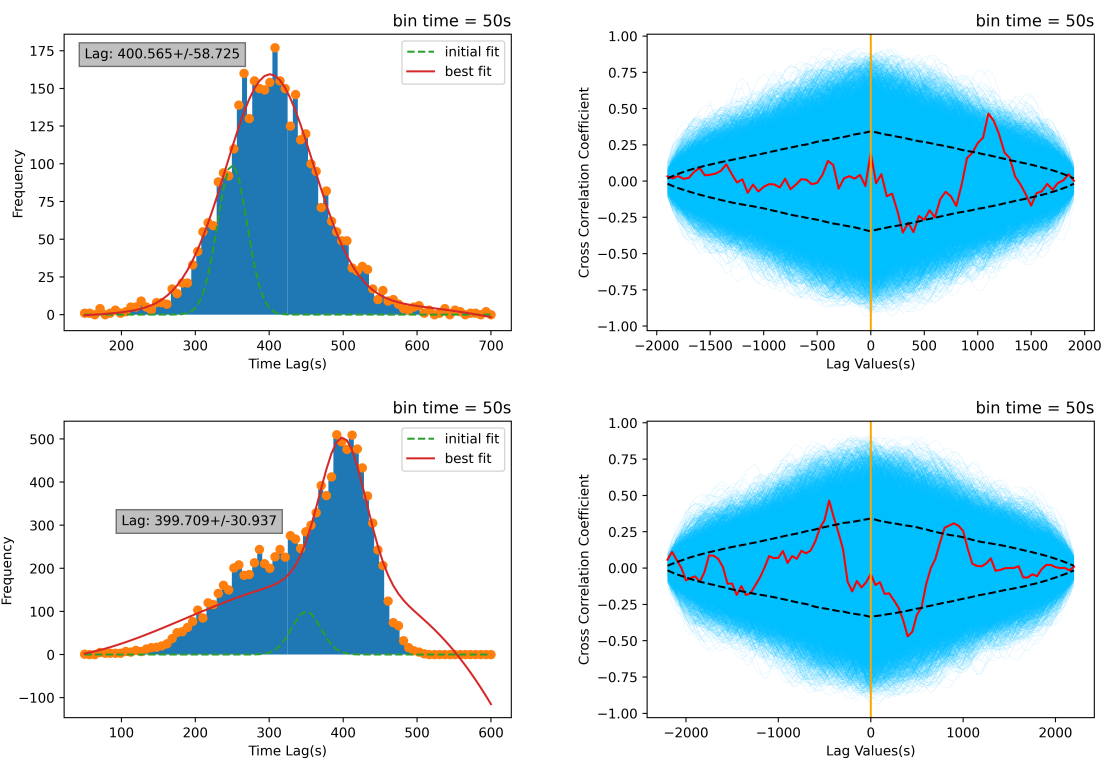


Figure 5: In each row, the left plot is of the histogram of the simulated CCFs and the right plot is of the associated Confidence Interval for that section using LCs simulated with the Timmer-Konig method. 1995 method, where the 95% confidence windows are shown with the black dotted line and the simulated CCF plots are shown in a blue shaded area. The red colour plot overlayed is of the observed CCF.

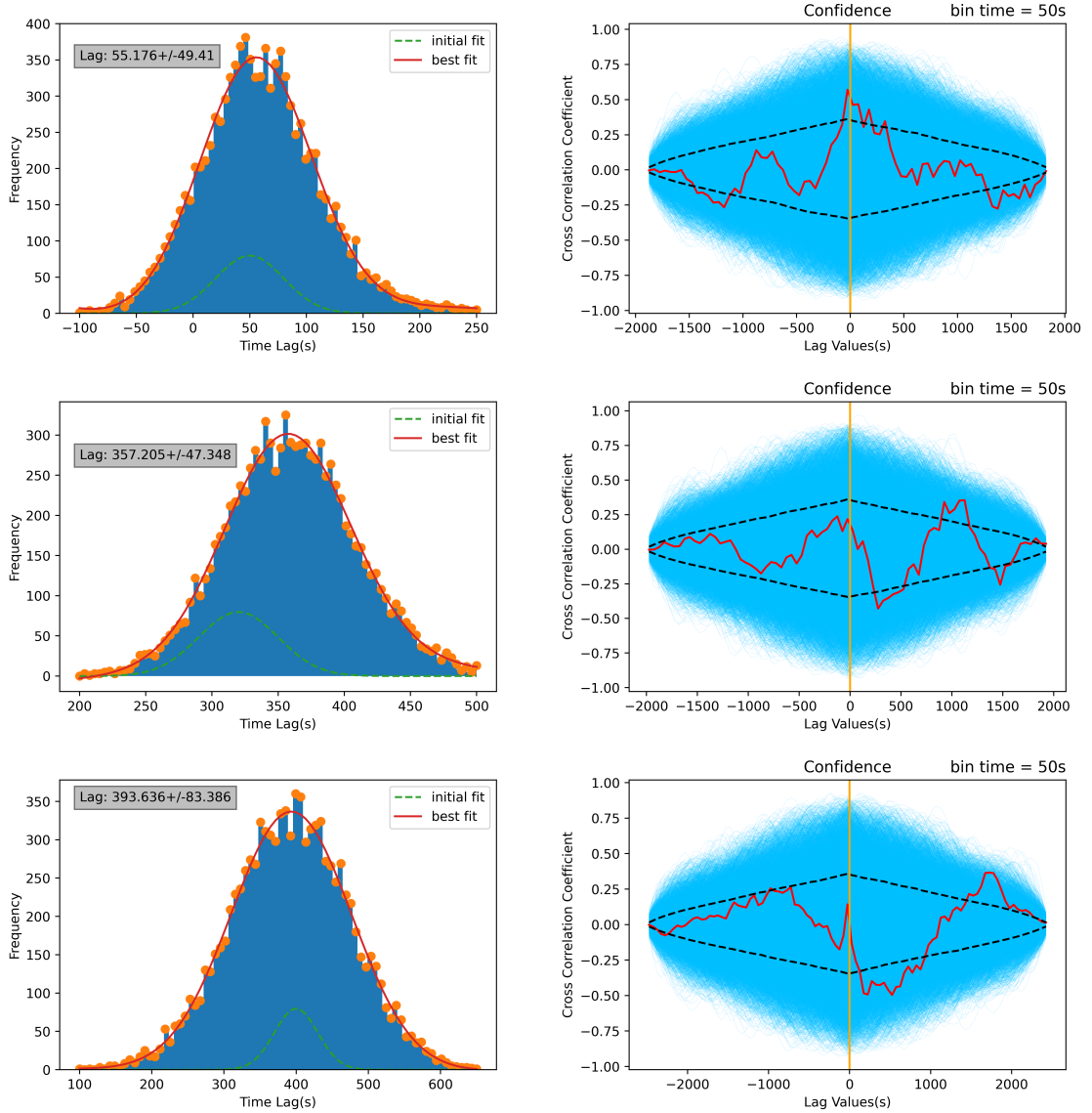


Figure 6: Simulated CCFs histogram (left) and associated Confidence Interval plots (right) using Timmer-Konig method (1995), the 95% confidence windows shown with the black dotted line and the simulated CCF plots shown in a blue shaded area. The red color is the observed CCFs for sections A and B in rows 1 and 2, respectively.

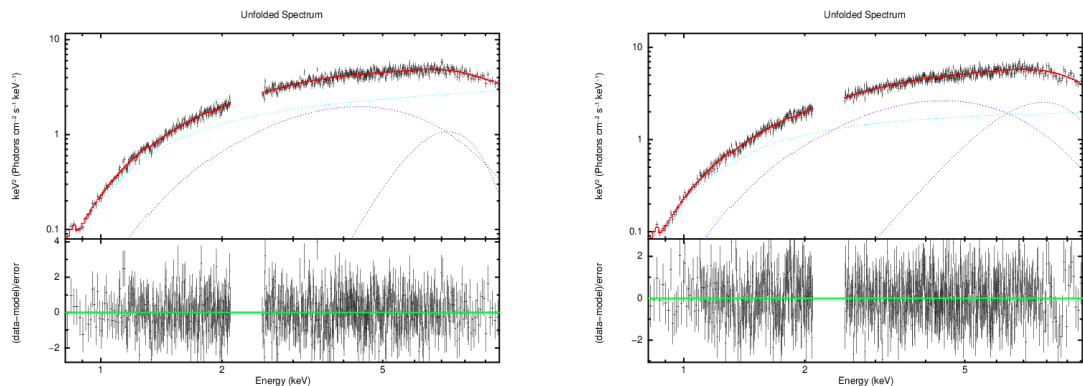


Figure 7: Spectrum of Section A, fitted with model 1; First 500 s (left), Last 500 s (right).

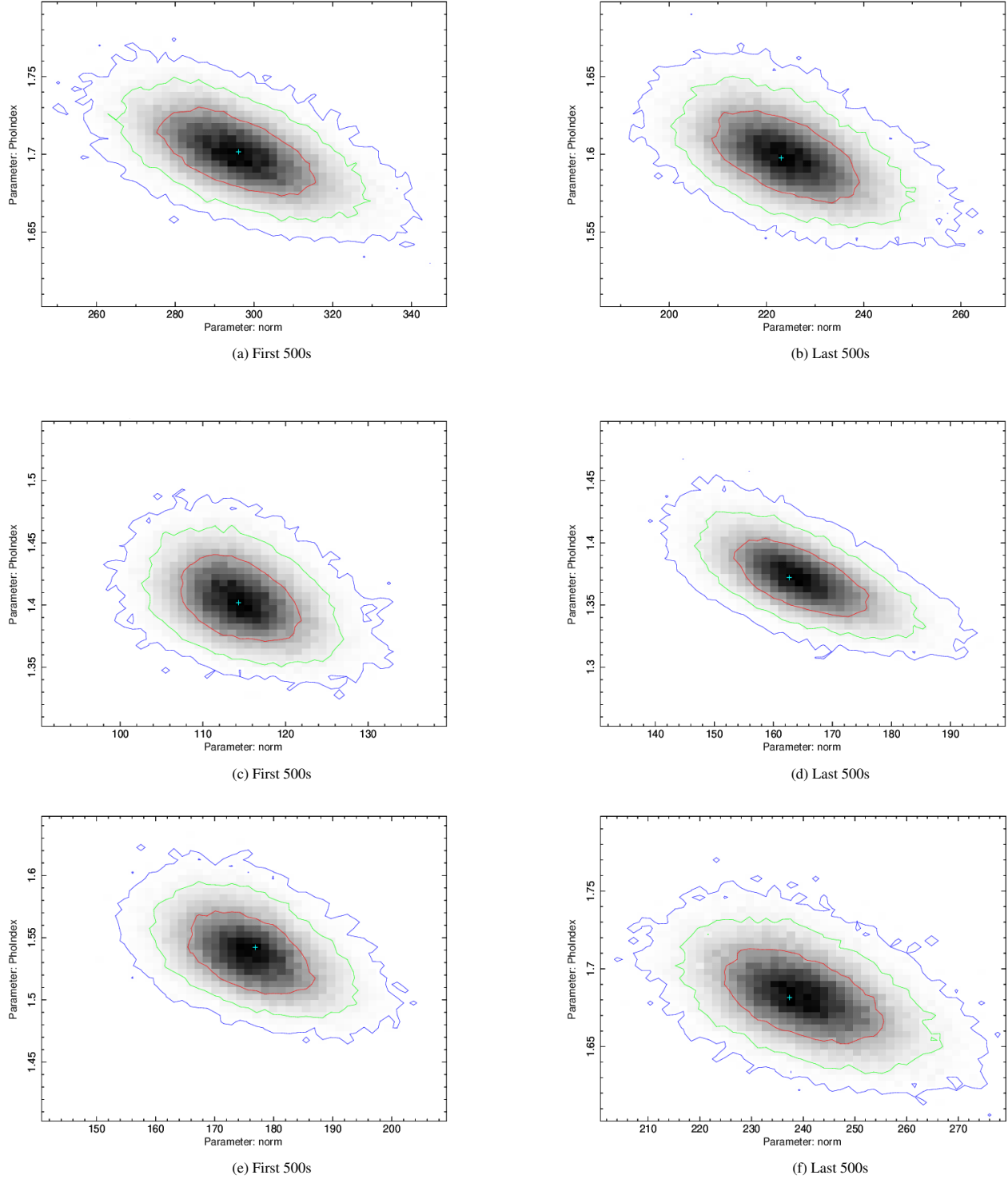


Figure 8: Section A, B, and C Contour plots of **Norm of bbodyrad** vs Γ of **Power-law model**, from Model 1 ($Tbabs * (bbodyrad + power-law + Gaussian)$), where in each row, the left plot is of the First 500s of that section and the right plot is of the Last 500s of that section.